ACADEMIC PRESS

Available online at www.sciencedirect.com
SCIENCE DIRECT®

Journal of Catalysis 213 (2003) 163–175

JOURNAL OF CATALYSIS

www.elsevier.com/locate/jcat

High loading of short WS_2 slabs inside SBA-15: promotion with nickel and performance in hydrodesulfurization and hydrogenation

L. Vradman,[a] M.V. Landau,[a,*] M. Herskowitz,[a] V. Ezersky,[b] M. Talianker,[b] S. Nikitenko,[c] Y. Koltypin,[c] and A. Gedanken[c]

[a] *Blechner Center for Industrial Catalysis and Process Development, Department of Chemical Engineering, Ben-Gurion University of the Negev, Beer-Sheva 84105, Israel*

[b] *Department of Materials Engineering, Ben-Gurion University of the Negev, Beer-Sheva 84105, Israel*

[c] *Department of Chemistry, Bar-Ilan University, Ramat-Gan 52900, Israel*

Received 13 May 2002; revised 16 August 2002; accepted 24 August 2002

Abstract

Layered nanoslabs of a WS_2 phase with a well-defined hexagonal crystalline structure, average slab length of 3.6 nm, and stacking number of 3.2 were inserted into the nanotubular channels of SBA-15, an ordered pure silica material (surface area of 800 m^2/g, uniform mesopore diameter of 6.5 nm) at loadings up to 60 wt.%. Sonication of a slurry containing SBA-15 in a $W(CO)_6$–sulfur–diphenylmethane solution yielded an amorphous WS_2 phase inside the mesopores. By sulfidation with 1.5% dimethyldisulfide in toluene under a hydrogen flow at 593 K and 5.4 MPa, the amorphous phase was transformed into hexagonal crystalline WS_2 nanoslabs (as shown by XRD, HRTEM, and selected area electron diffraction (SAED)). The WS_2 nanoslabs were distributed exclusively inside the mesopores in a uniform manner (HRTEM, quantitative microanalysis), without blocking the pores (N_2-sorption), and were oriented with their edge planes toward the support surface. This study constitutes the first report of such a combination of high loading of a well-defined crystalline catalytic phase into the nanotubular channels of mesoporous silica without blocking them. The first well-resolved HRTEM images of the well-defined crystalline catalytic phase (WS_2) inside the SBA-15 nanotubes are presented. A Ni component was introduced into the WS_2/SBA-15 composite by impregnation from an aqueous solution of nickel acetate. It increased the catalytic activity up to a Ni/W ratio of 0.4. In the hydrodesulfurization (HDS) of dibenzothiophene and the hydrogenation (HYD) of toluene, the activity of the optimized Ni–W–S/SBA-15 catalyst was 1.4 and 7.3 times higher, respectively, than that of a sulfided commercial Co–Mo/Al_2O_3. This finding illustrates the excellent potential of high loading Ni–W–S/SBA-15 catalysts for deep hydrotreatment of petroleum feedstocks.

Keywords: Mesoporous silica; WS_2; Nanoslabs; Nickel; Hydrodesulfurization; Hydrogenation

1. Introduction

The potential applications of ordered mesoporous silicas with pore walls of uniform width in the range 1–5 nm and controlled uniform pore diameters in the range 2.5–25 nm [1–3] as periodic hosts for the preparation of mesoporous catalysts with chemically functionalized surfaces have been widely investigated in the past decade [4–6]. Much less attention has been paid to the preparation of catalytic mesoporous silicas with inclusions of nanocrystals of well-defined catalytic phases [7]. This neglect is indeed surprising in the light of the numerous examples in catalytic practice in which efficient active sites created at the surfaces of such phases (due to optimized geometrical arrangement of the atoms) do not have molecular analogs with similar performance. The best known of these phases are TiO_2 anatase as a photocatalyst and a basis for vanadium oxide catalysts in selective oxidations [8,9], tetragonal ZrO_2 as a basis for superacidic sulfated zirconia [10–12], layered $Mo(W)S_2$ slabs with Co(Ni)-ions decorating their edge planes in hydrotreating catalysis [13–15], acidic zeolite catalysts [16], and heteropoly compounds in acidic and redox catalysis [17]. The potential advantage of mesoporous silica hosts for the preparation of catalytic phase materials lies in the high dispersion of the catalytic phase at high loadings that, depending on the nature of the host, may

* Corresponding author.
E-mail address: mlandau@bgumail.bgu.ac.il (M.V. Landau).

0021-9517/02/$ – see front matter
PII: S0021-9517(02)00012-X

surpass 30–60 wt.%—a combination that cannot be achieved with conventional supports having textural porosity, such as silica gel or precipitated aluminas.

To take full advantage of ordered mesoporous silicas for the preparation of included catalytic phase dispersions, three main conditions must be fulfilled:

- the entire catalytic phase must be located inside the pore system of the mesoporous host;
- the nanoparticles must have a well-defined optimized crystal structure; and
- there must be minimal blocking of the host's pore system by the catalytic phase dispersions at high loading.

The few attempts that have been made up to the present to prepare high-loading (> 30 wt.%) catalytic phase dispersions inside mesoporous silica hosts [18–23] have shown that simultaneous accomplishment of these three goals is a very complicated problem.

The multistep impregnation of the hexagonal 1D mesoporous silica SBA-15 with an aqueous Y–Eu-nitrate solution (Y/Eu = 32.3) yielded a material in which most of the Y_2O_3 phase, at loadings up to 22 wt.%, was spread as an amorphous monolayer coating the internal pore surfaces [7,18]. In a high-loading material (35 wt.% Y_2O_3), Y_2O_3 was present in three different forms: in addition to the oxide monolayer, oxide nanoparticles were detected inside the pores (HRTEM) and large cubic Y_2O_3 crystals (18 nm (XRD)) outside the silica particles [18]. The blocking extent (BE) of the silica mesopores for this high-loading material was relatively high (i.e., BE ≈ 0.65). BE was calculated by us as BE $= 1 -$ NSA, where NSA, the normalized surface area, was defined as $\mathrm{NSA} = \mathrm{SA}_{\mathrm{composite}}/\mathrm{SA}_{\mathrm{pure\ silica}}(1-y)$, in which y is the weight fraction of the guest component in the composite material [23]. The multistep impregnation of cubic silica MCM-48 with aqueous Fe-nitrate facilitated the synthesis of a high-loading composite material (42.5 wt.% Fe_2O_3) in which the entire host phase was located inside the silica pore system, as shown by HRTEM [19]. The pore BE (0.35) was significant, but relatively low due to the 2D pore system, and the host phase existed in the form of disordered iron oxide nanoparticles with less strong linking of the FeO_6 octahedra relative to the well-defined hematite phase (EXAFS). One-step impregnation of MCM-41 with an aqueous solution of the heteropolyacid $H_3PW_{12}O_{40}$ yielded a composite with 33 wt.% loading that contained both grafted heteropolyacid anions (FTIR) and crystals of the heteropolyacid phase (XRD) with a high pore BE ≈ 0.7 [20]. The catalytic activity of this composite in the cracking of 1,3,5-triisopropylbenzene increased with increasing heteropolyacid loading and passed through a sharp maximum at 23 wt.%. The multistep grafting with aluminum butoxide of MCM-41, in which the pores had been expanded by addition of mesitylene to the surfactant, facilitated the synthesis of a composite with 38 wt.% alumina loading and no pore blocking [21]. The catalytic activity of the host amorphous alumina phase in the alkylation of phenol with methanol was about five times that of the reference material—bulk alumina [21]—due to a substantially higher population of acidic pentahedral aluminum atoms, as shown by ^{27}Al FAM(II)-MQMAS NMR [22]. Ultrasonication of a slurry of wide-pore (expanded) MCM-41 in a $Mo(CO)_6$–decaline solution yielded a composite with 45 wt.% MoO_3 loading, in which the guest phase was spread as an amorphous monolayer coating the internal pore surfaces (HRTEM, XPS, MAS NMR) with a minimal pore BE of 0.07 [23].

It is possible to control the distribution mode of the catalytic phase (spreading or nanoparticle formation) at high loadings by varying the nature of the guest precursor and the method of insertion. However, to date, the fulfillment of all three conditions delineated above in an optimized host/guest catalytic composite has not yet been achieved with any system. The main problem is to combine the formation of a well-defined nanocrystalline catalytic phase inside the mesopores with uniform distribution of the nanocrystals in the pore volumes and high accessibility of the nanocrystals to the reacting molecules (i.e., low BE).

The purpose of this study was to address the above-described problem by investigating, as a model system, the insertion of a layered WS_2 phase into SBA-15 mesopores. The new catalyst was designed on the basis of available knowledge about the sulfide catalyst $Mo(W)S_2$. It is known that the active sites of the sulfide catalyst are located in the edge planes of $Mo(W)S_2$ slabs [13–15]. It is generally agreed that the shorter the slabs, the higher the fraction of edge planes and hence the higher the catalyst activity. Recently, it was found that the stacking degree of supported $Mo(W)S_2$ slabs plays an important role in the catalytic performance of sulfide catalysts; i.e., it determines the activity of the catalyst in the hydrogenation (HYD) of aromatics [24,25]. The orientation of the $Mo(W)S_2$ slabs relative to the support surface also seems to have an influence on the catalytic activity [14,26]. The underlying premise of the current study was therefore that the highly ordered porosity of the SBA-15 support would provide a way of controlling the structure (length and stacking degree) and orientation of the metal sulfide nanocrystals at high loading.

It has previously been shown that ultrasonication of a solution of $Mo(CO)_6$ in decalin in the presence of dissolved oxygen yielded a Mo phase spread as an amorphous monolayer coating the internal pore surfaces of MCM-41 [23]. The amorphous Mo monolayer was formed by interaction between coordinatively unsaturated Mo species (produced by ultrasonically induced decarbonylation) and surface silanols and siloxane bridges [23,27]. In our catalyst system, the amorphous WS_2 phase was prepared directly by ultrasound irradiation of a solution of $W(CO)_6$ in diphenylmethane in the presence of dissolved elemental sulfur under argon at 90 °C [28]. To avoid spreading of the WS_2 phase, an excess of sulfur was used during ultrasonic deposition of WS_2 on the SBA-15 support. Further thermal treatment of this amorphous WS_2 phase in a hydrogen sulfide/hydrogen

atmosphere converted it to layered WS_2 nanocrystals. The location, structure, and orientation of the WS_2 slabs were studied by HRTEM, XRD, SAED, N_2-sorption, and qualitative microanalysis (EDS). The promotion of these slabs with Ni and the catalytic performance of the final product in the HYD of toluene and the HDS of dibenzothiophene (DBT) were also investigated.

2. Experimental

2.1. Catalyst preparation

The preparation of SBA-15 was first reported in 1998 [29], but we used a subsequently published method [30], which gives better reproducibility of the hexagonal porous array. In a typical procedure, 14.0 g of poly(ethylene glycol)-*block*-poly(propylene glycol)-*block*-poly(ethylene glycol) triblock copolymer (Aldrich, $H(–OCH_2CH_2)_x[–OCH(CH_3)–CH_2–]_y(–OCH_2CH_2–)_zOH$, $M_{avg} = 5800$) was dissolved with stirring in 447 ml of water and 66 ml of 32 wt.% HCl for 1 h at 50 °C, followed by addition of 21.7 g of tetramethylorthosilicate with stirring for 10 min. The solution was then transferred into a Teflon reactor and stirred first at 60 °C for 24 h and then at 100 °C for 24 h. After cooling to room temperature, the solid product was recovered by filtering without washing and drying in air at room temperature for 16 h and at 100 °C for 2 h. Calcination at 300 °C for 2 h, 400 °C for 2 h, and 500 °C for 6 h (with a slow temperature increase of 1 °C/min) completed the preparation. The BET surface area of the prepared material varied in the range of 800–1300 m^2/g with similar d-spacings and mesopore diameters. This was a result of the formation of microporous coronas in the walls of the mesopores [31] that comprise up to 45% of the total surface area (t-plot). The preparation procedure was therefore modified to reduce the microporosity; this was achieved according to [31] by increasing the duration of the hydrothermal treatment at 100 °C to 3–7 days instead of 24 h before recovery by filtration. The SBA-15 samples prepared in such a way had a BET surface area of 800–1000 m^2/g and the contribution of the micropores to the total surface area decreased to $< 25\%$. This modified procedure was used in the present study for preparation of SBA-15.

Diphenylmethane (> 99%, Fluka) and $W(CO)_6$ (97%, Aldrich) were used without further purification. Typically, 12 mmol of $W(CO)_6$, 26 mmol of elemental sulfur (Aldrich), and 0.5 g of freshly calcined SBA-15 (500 °C) were introduced to 80 ml of diphenylmethane and heated to 90 °C under stirring in an argon flow for 1 h. Changing the concentrations of $W(CO)_6$ and elemental sulfur facilitated control of the WS_2 content in the final product. The slurry was sonicated at 90 °C for 3 h under argon with a high-intensity ultrasonic probe (Sonics & Materials VCX 600 Sonifier, 1 cm^2 diameter titanium horn, 20 kHz, 40 $W\,cm^{-1}$). In a N_2-filled glove-box, the black solid product was removed by centrifugation, washed once with toluene and twice with dry pentane, and dried under vacuum at room temperature. The dried solid was transferred to the tubular reactor and sulfidated in situ with a 1.5% dimethyldisulfide (DMDS)-toluene mixture at 320 °C and 5.4 MPa under hydrogen flow for 24 h. Unsupported WS_2 was prepared in the same way without addition of SBA-15 to the sonicated solution.

The WS_2/SBA-15 composite was characterized by FTIR. The absence of peaks in the region of 2000 cm^{-1}, corresponding to the C–O stretching vibrational mode, indicated that no W-carbonyl precursor was present in the final solid product. Similarly, the disappearance of absorption bands at 3060–3020 and 2900–2850 cm^{-1}, assigned to C–H stretching vibrations in aromatic and aliphatic groups, respectively, indicated that the hydrogenation–sulfidation treatment had destroyed any diphenylmethane polymers that might have been formed during sonication [28].

The Ni component was introduced into the WS_2/SBA-15 composite after sulfidation by impregnation with an aqueous solution of nickel acetate and drying under vacuum at room temperature, followed by additional sulfidation performed as described above. As shown previously [32], this method of Ni introduction into a Mo-sulfide phase provides high Ni dispersion with consequent enhancement of the catalytic activity in HDS.

For preparation of reference Ni–W catalysts, two commercial supports were used: γ-alumina (Norton SA 6175, cylinders $d = 1.3$ mm, BET surface area 270 m^2/g, pore volume 0.65 cm^3/g) and silica gel (PQ CS-1030E, cylinders $d = 1.7$ mm, BET surface area 300 m^2/g, pore volume 1.0 cm^3/g). The catalysts were prepared by wet impregnation of the support with an aqueous solution of nickel nitrate and ammonium tungstate, followed by drying and sulfidation, as reported previously [24]. Commercial Co–Mo/Al_2O_3 catalyst KF-752 (Akzo Nobel Chemicals) was used after sulfidation as a reference sample in testing experiments. The commercial catalyst and the catalysts prepared by Ni–W impregnation of commercial γ-alumina and silica were used in the actual shape and size produced. Pelletization of powdered Ni–W–S catalysts deposited on SBA-15 was accomplished by pressing the material at 1.4×10^3 kg/cm^2, followed by crushing and separation of a fraction with average pellet diameter of 1.3 mm.

2.2. Catalyst characterization

Small-angle X-ray scattering (SAXS) patterns were obtained with Ni-filtered Cu-K_α radiation (SEIFERT ID 3000 generator), which was directed through an evacuated compact Kratky camera (Anton PAAR) onto the sample placed in a 1.5-mm diameter glass capillary (GLAS). A linear position-sensitive detector (MBRAUN) was used to record the scattering patterns. The scattering curves were normalized with respect to the attenuated main beam.

The chemical composition of the solid catalysts (in wt.%, average of five measurements at different points of the

solid) was obtained by energy dispersive X-ray spectroscopy (EDS) analysis with a JEOL JEM 5600 scanning electron microscope. Surface areas, pore volumes, and pore size distributions were obtained from N_2 adsorption–desorption isotherms using conventional BET and BJH methods. The samples were outgassed under vacuum at 250 °C. Isotherms were obtained at the temperature of liquid nitrogen with a NOVA-1000 (Quantachrome, Version 5.01) instrument. FTIR spectra of the catalyst materials were recorded on a Nicolet (Impact 4) spectrometer. Conventional wide-angle XRD patterns were obtained on a Phillips diffractometer PW 1050/70 (Cu-K_α radiation) equipped with a graphite monochromator using software developed by Crystal Logic. The data were recorded with a 0.02° step size, 2 s at each step. HRTEM micrographs were obtained on a JEOL FasTEM-2010 electron microscope operating at 200 kV and equipped with an analytical EDS system for composition analysis. A probe size of ∼ 15–20 nm was used for the determination of Ni, W, and Si content in the particles. The TEM samples were prepared by depositing a drop of an ultrasonicated ethanol suspension of solid catalyst on a carbon-coated Cu grid. The grid was dried at room temperature under vacuum and mounted into a specimen holder. Samples were examined as grain mounts. The statistical analysis of WS_2 particles was performed on data obtained from 10 different places (100×100 nm^2) on the sample. The average particle length L was calculated according to the first moment of distribution, $L = \sum_{i=1}^{m} m_i l_i / \sum_{i=1}^{m} m_i$, where l is the length of the slab along the basal plane, as determined directly from HRTEM micrographs, and m is the number of particles measured in the specific size range. The average stacking number F was calculated in the same manner using stacking number f instead of l in the first moment of the distribution equation. Phase-contrast HRTEM images from the thinnest areas of the sample were obtained with a removed objective aperture at under-focus conditions close to the Scherzer defocus in order to provide optimum contrast and best resolution.

2.3. Catalyst testing

Catalyst performance was evaluated in a high-pressure fixed-bed reactor minipilot unit, controlled automatically by a PC, as described in detail elsewhere [33]. In the evaluation experiments, 5 cm^3 of catalyst mixed with 10 cm^3 of 0.2-mm silicon carbide particles (Norton Co.) were packed into a 12-mm i.d. stainless steel tubular reactor between two 10-cm layers of 0.2-mm diameter silicon carbide particles. All tests were performed with catalysts sulfided for 24 h with a 1.5% DMDS–toluene mixture at LHSV = 2.5 h^{-1}, 593 K, a hydrogen pressure of 5.4 MPa, and a H_2/toluene ratio 500 NL/L.

HDS of DBT was carried out with 1 wt.% DBT dissolved in equal quantities (wt.%) of n-decane and n-octadecane at 593 K, hydrogen pressure 3.1 MPa, H_2/liquid ratio of 500 NL/L, and LHSV in the range 40–120 h^{-1}. The HDS products were analyzed by GC using a Chrompack 9001 instrument equipped with a flame ionization detector and a CP-Sil5 CB capillary column 10 m long with i.d. 0.255 mm. No sulfur-containing substances other than unconverted DBT were detected in products. DBT was converted to biphenyl- and cyclohexylbenzene. Under the tested operating conditions, the rate of HDS of DBT fitted pseudo-zero-order HDS kinetics [23]. The rate constants were calculated according to the equation $k_{HDS} = x_{DBT}{}^{*}\text{LHSV}$, where $k_{HDS} = k/C_0$ (C_0—inlet DBT concentration, k—pseudo-zero-order HDS rate constant), and x_{DBT} is the conversion of DBT. The HDS rate was also calculated as the turnover number [TON (h^{-1})], defined as the amount of reacted DBT molecules per hour normalized per number of W (Mo) atoms loaded in reactor with the catalyst sample. TON characterizes the HDS efficiency of the W (Mo)-phase promoted with Ni (Co), since the Ni (Co)-sulfide phase itself is almost inert in HDS [13,14].

The toluene HYD experiments were conducted with a 1.5% DMDS–toluene mixture at 628 K, hydrogen pressure 5.4 MPa, and H_2/toluene ratio of 1500 NL/L. The toluene to methylcyclohexane conversion (x_{tol}) was measured using the same GC equipment as for DBT HDS products. The HYD rate of toluene fitted pseudo-first order kinetics as reported previously [34]. The toluene HYD rate constants were calculated according to the equation $k_{HYD} = \text{LHSV} * \ln(1 - x_{tol})^{-1}$.

3. Results and discussion

3.1. Characterization of WS_2/SBA-15 samples

Figure 1 presents SAXS patterns of the synthesized SBA-15 material. The high-intensity first peak (100) has a d-spacing of 10.3 nm and the following peaks have d-values consistent with a hexagonal arrangement of the pores with the distance of 11.9 nm. These findings confirm that SBA-15 has a well-defined hexagonal pore structure, in agreement with previous studies [29,30].

Figure 2a shows the N_2 adsorption–desorption isotherms for the parent SBA-15 material and for SBA-15 loaded with 20 or 60 wt.% WS_2 by ultrasonication (A, B, and C, respectively). The uniform mesopore diameter of the parent SBA-15 material is equal to 6.5 nm (Fig. 2b, curve A, BJH method). Taking into account the distance between pores measured by SAXS, we calculate the pore wall thickness of SBA-15 to be equal to $11.9 - 6.5 = 5.4$ nm.

Loading of WS_2 into SBA-15 led to a marked change in the shape of the hysteresis loop and reduction of the pore volume (Fig. 2a, curves B and C). The hysteresis loop of the loaded material was characteristic of a percolation effect caused by small WS_2 particles settling within the mesopores, effectively forming ink-bottle type pores [7]. The broadening of the BJH pore size distribution and the small shift to the lower pore diameter (Fig. 2b) in the WS_2-

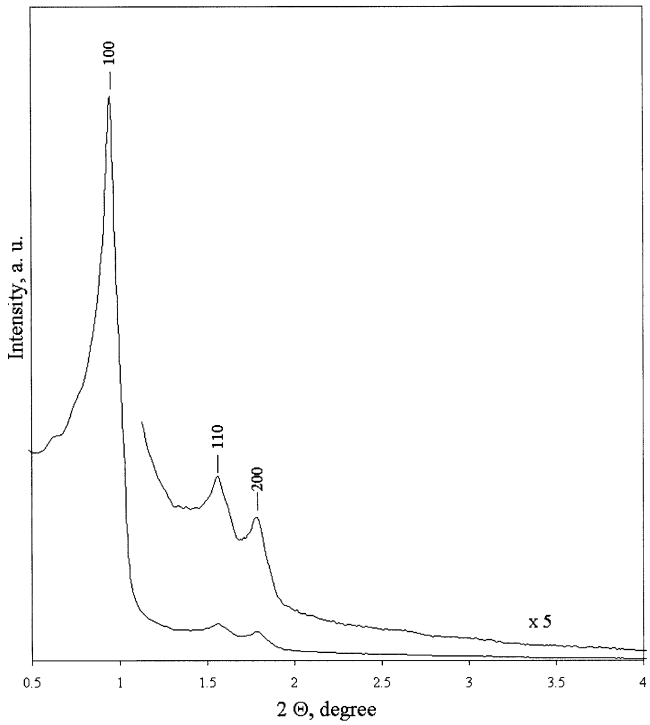

Fig. 1. SAXS profile of SBA-15.

containing samples relative to parent SBA-15 also reflected the formation of particles inside the pores.

The pore volumes and BET surface areas of the parent SBA-15 material and of the WS_2/SBA-15 composite materials are listed in Table 1. The surface areas normalized per weight of silica and the normalized pore volumes of the samples were calculated as described in the Introduction [23]. The normalized surface area and pore volumes were high for both loaded samples, which is evident for the relatively small pore blocking effect (Table 1). Increasing the WS_2 loading beyond 60 wt.% led to significant pore blocking. Assuming that the density of the WS_2 phase inside the SBA-15 nanotubes was close to the density of natural tungstenite (7.5 g/cm^3 [35]), the volume of the WS_2 phase in 1 g of 60 wt.% WS_2/SBA-15 ($0.6 \times 1/7.5 = 0.08$ cm^3) was relatively small compared to the pore volume of SBA-15 in the same sample ($1 \times 0.4 = 0.4$ cm^3), but it could explain the small reduction of the normalized pore volume (Table 1). The BET surface area of bulk WS_2 prepared by ultrasonication in the absence of SBA-15 (60 m^2/g) was much lower than that of SBA-15 or that of WS_2/SBA-15 samples.

Figure 3 (traces a, b, c, and d, respectively) shows XRD patterns for the parent SBA-15, 60 wt.% WS_2/SBA-15 (after sonication), 60 wt.% WS_2/SBA-15, and Ni–W–S/SBA-15 with Ni/W ratio of 0.8, both treated with a DMDS-toluene mixture under hydrogen. The broad peak at about $2\Theta = 24°$, corresponding to amorphous silica (Fig. 3a), almost disappeared after ultrasonic deposition of 60 wt.% WS_2; this is particularly pronounced in Fig. 3c. The disappearance of this peak was attributed to the dilution of amorphous silica with a high percentage of tungsten ions, which have a higher adsorption factor for X-rays than silicon. Hence, the broad peaks evident in Fig. 3b could be attributed to the ultrasonically deposited amorphous WS_2 phase. Treatment with the DMDS–toluene mixture under hydrogen led to the formation of small crystals of a hexagonal WS_2 phase, as follows from the good correlation between the broad peaks in Fig. 3c with peaks for crystalline hexagonal WS_2. Furthermore, the broad peak at about $2\Theta = 27°$ in Fig. 3b is not present in Fig. 3c; this finding suggests that the entire amorphous WS_2 phase had been converted to crystalline hexagonal WS_2. It is widely accepted that the active sites of Mo(W)-based hydrotreating catalysts are located at the edge plans of the layered hexagonal Mo(W)S_2 phase [13]. Therefore, by analogy, treatment of the ultrasonically deposited amorphous WS_2 phase with the DMDS–toluene mixture under hydrogen was essential to produce the crystalline phase active in hydrotreatment. All subsequent characterizations were thus performed with the treated samples. It can be also seen from Fig. 3d that introduction of Ni slightly improved the crystallinity of WS_2 phase, as was reflected by minor changes in the diffractogram of the WS_2/SBA-15 composite. The fact that no new reflections were detected implies high dispersion of the Ni component, which probably decorates the edge plans of the WS_2 slabs.

Direct evidence for the location the WS_2 phase nanocrystals within the SBA-15 nanotubes, with no spreading of the WS_2 phase, was obtained by HRTEM. TEM micrographs, taken from the 60% WS_2/SBA-15 sample along two perpendicular directions, show the mesoporous structure of the SBA-15 support (Figs. 4a and 4b). The hexagonal ordered system of the nanotubes is clearly evident in Fig. 4b, in which the nanotubes lie parallel to the electron beam. The distance between adjacent tubes is about 11.5 nm, and the pore wall thickness is about 5 nm, in agreement with the calculations based on SAXS and N_2-sorption data.

HRTEM micrographs taken at high magnification unambiguously show the nanoparticles occluded within the nanotubes (Figs. 4c and 4d). Parallel fringes running across the nanoparticle images have a periodicity of 6.2 Å, which corresponds to the well-known distance of 6.13 Å between the atomic layers packed along the c-axis in the hexagonal WS_2 structure (JCPDS, file number 8-237, $a = 3.154$ Å, $c = 12.362$ Å [36]). The HRTEM image in Fig. 4c represents a side view of the nanotubes with similar nanoparticles appearing inside them. An electron diffraction pattern taken from the large area of the specimen exhibits a few faint rings corresponding to planes (101) and (110) with d-spacings equal to $d_{101} = 2.67$ Å and $d_{110} = 1.57$ Å, respectively (Fig. 5). These values match the interplanar distances characteristic of the hexagonal WS_2 structure.

All these observations suggest that the nanoparticles located within the nanotubes have the layered structure of a well-crystallized WS_2 phase. This conclusion is in line with the results of EDS analysis of the area containing the nanoparticles. A typical EDS spectrum obtained with a 15-nm nanoprobe revealed the presence of W and S

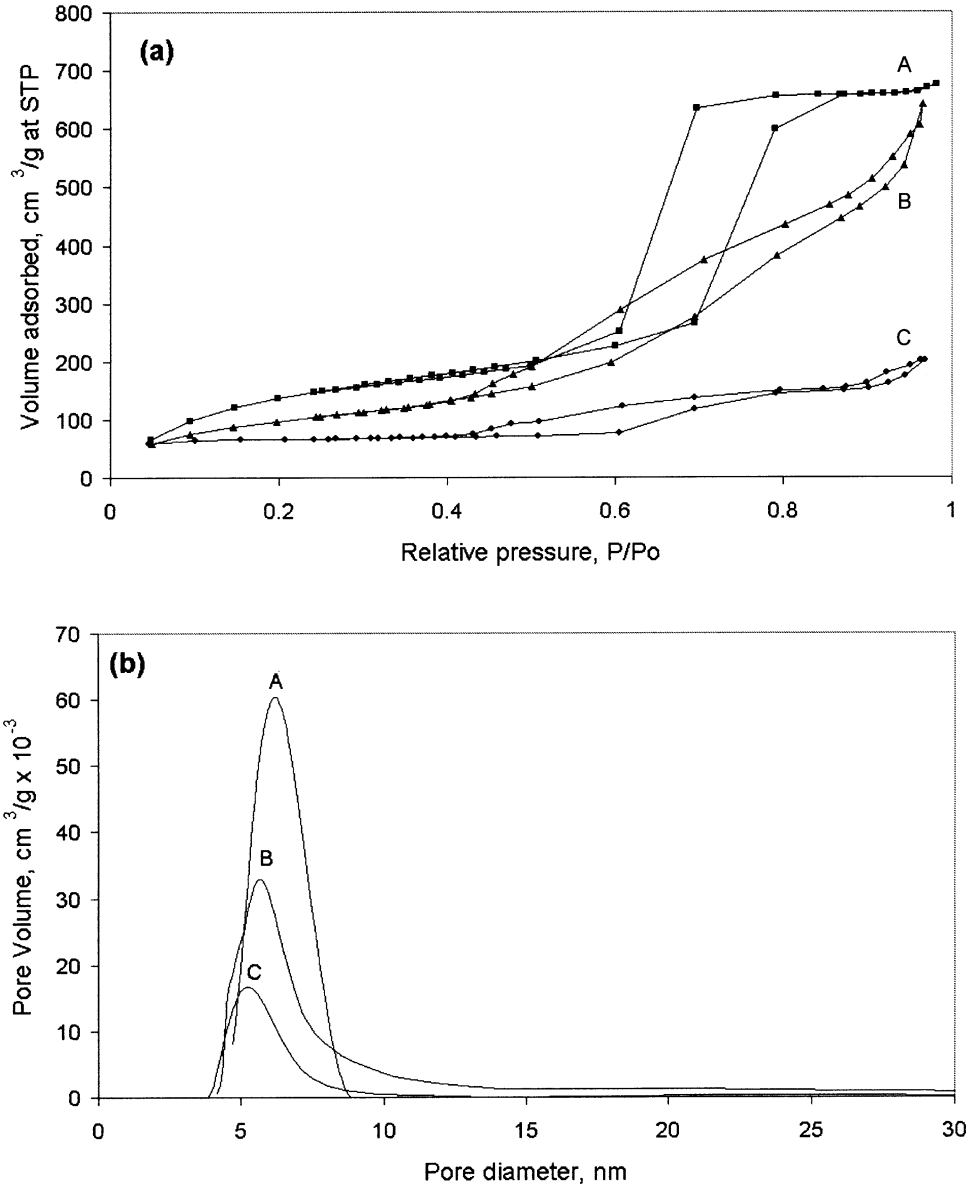

Fig. 2. Nitrogen sorption isotherms (a) and pore size distribution (b) of parent SBA-15 (A), 20 wt.% WS_2/SBA-15 (B), 60 wt.% WS_2/SBA-15 (C).

peaks, in addition to the Si and O peaks of silica (see Fig. 6). Quantitative analysis gave an S/W atomic ratio close to 2, thus leaving little doubt that the observed nanoparticles can be ascribed to the WS_2 phase. The average EDS analysis collected from the different points gave WS_2 concentration (average of 10 measurements) similar to the averaged composition measured by SEM-EDS. Furthermore, an examination of 15 different 85 × 85-μm areas of the sample indicated no WS_2 phase outside the SBA-15 particles. Thus the nanocrystals of the WS_2 phase were located inside the mesopores of the SBA-15 support. HRTEM was used to measure particle length and stacking number of each WS_2 particle. Statistical treatment of the data for hundreds of WS_2 particles taken from 10 different places (100 nm × 100 nm) in the sample yielded an average stacking number of 3.2 and an average length of 3.6 nm.

Table 1
Texture of SBA-15 and WS_2/SBA-15 samples derived from N_2-sorption

Sample	Pore volume		BET surface area	
	cm^3/g	Normalized	m^2/g	Normalized
SBA-15	1.0	1.0	800	1.0
20% WS_2/SBA-15	0.68	0.85	509	0.80
60% WS_2/SBA-15	0.28	0.70	230	0.72

Normalized$(X) = X_{\text{catalyst}}/((1-y)X_{\text{SBA-15}})$, where X is specific surface area or pore volume and y is weight fraction of WS_2 in the catalyst.

SAXS of WS_2/SBA-15 composite did not display any reflections. Generally, reduction of the reflections may be caused by three reasons: (1) degradation of the hexagonal arrangement of SBA-15 pores, (2) dilution of silica with a high percentage of tungsten, which has a higher adsorption factor for X-rays than silicon, (3) formation of WS_2 nanopar-

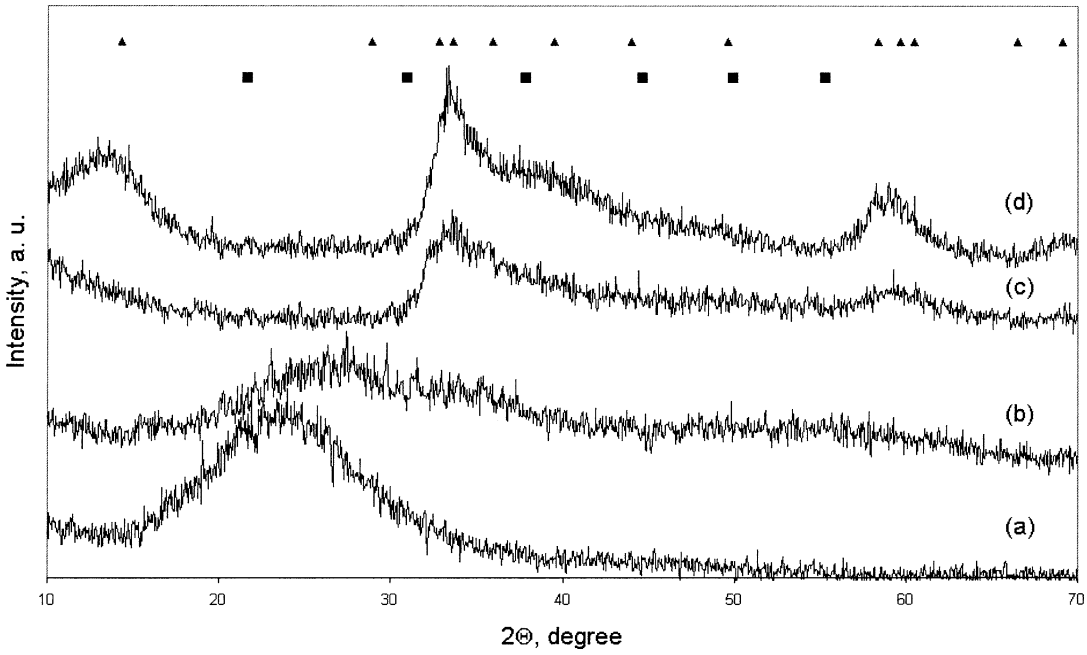

Fig. 3. XRD diffractograms of parent SBA-15 (a), 60 wt.% WS_2/SBA-15 after sonication (b), 60 wt.% WS_2/SBA-15 treated with DMDS–toluene mixture under hydrogen (c), and Ni–W–S/SBA-15 with a Ni/W ratio of 0.8 treated with DMDS–toluene mixture under hydrogen (d). The triangles and squares signify the reflections of crystalline hexagonal WS_2 phase (JCPDS, file number 8-237, [36]) and the crystalline Ni_3S_2 phase (JCPDS, file number 8-126, [36]), respectively.

ticles inside the pores and not spreading of the WS_2 phase along the pore walls [37]. The hexagonal arrangement of the SBA-15 pores was retained after WS_2 insertion, as could be seen from HRTEM and N_2-adsorption data. The adsorption of X-rays by tungsten was indeed very significant, as follows from strong reduction of the main beam intensity. However, the extent of reduction of the d_{100} reflection intensity (up to the indetectable level) is much higher than the extent of reduction of the main beam intensity. This could be considered as the evidence for the formation of the WS_2 nanoparticles inside the nanopores rather than WS_2 phase spreading along the pore walls based on simulations of SAXS data made in [37], in agreement with our HRTEM data.

By extrapolation from a recent report for MoS_2 [15], it can be assumed that the WS_2 particles grow in the form of triangular slabs. Figure 7a shows a schematic representation of the inscribing mode of WS_2 nanoslabs orientated with their edge planes toward the walls of the nanotubes, as is consistent with HRTEM observations. Clear images of the WS_2 slabs only on the black stripes (pores of SBA-15) and fine contrast between pores and walls (Fig. 4c) could almost certainly be obtained if the composite WS_2/SBA-15 particle were very thin. Assuming a particle containing one row of the nanotubes (Fig. 7b), the mass of silica in a selected sample area S may be calculated as

$$M_{SiO_2} = \frac{\pi}{4}\left(H^2 - D^2\right) * B * n * \rho_{sil}, \tag{1}$$

where H is the distance between the pore axes, D is the pore diameter, B is the length of a pore in the selected sample area S, n is the number of pores in the selected sample area S, and ρ_{sil} is the density of SiO_2. For purposes of simplicity, the nanotube is assumed to have a cylindrical form, given the small difference between the volume of the wall and that of the hexagonal form of the nanotube. The average number of WS_2 slabs per unit of the sample area was calculated from data obtained from more than 10 different places, in analogy with Fig. 4c. Assuming a triangular form of the WS_2 slab and knowing the W–W distance in the slab [38], we calculated the mass of WS_2 as

$$M_{WS_2} = N * S * F * \frac{\sqrt{3}}{4}\left(\frac{L}{C}\right)^2 \frac{M_w}{A_v}, \tag{2}$$

where N is the average number of WS_2 slabs per unit of the sample area, S is the selected sample area, F is the average stacking number, L is the average slab length, C is the W–W distance in the slab, A_v is Avogadro's number, and M_w is the molecular weight of WS_2. It should be mentioned that the mass of WS_2 could be also calculated from its density and the volume determined from a measured slab length and stacking number,

$$M_{WS_2} = N * S * F * E * \frac{\sqrt{3}}{4}(L)^2 * \rho_{tun}, \tag{3}$$

where E is the distance between the atomic layers packed along the c-axis in the hexagonal WS_2 structure. The difference between the masses of WS_2 calculated from Eqs. (2) and (3) is less than 20%.

The estimation of the mass of silica from Eq. (1) and of the mass of WS_2 from Eq. (3) gives 12 wt.% WS_2 in the WS_2/SBA-15 sample, rather than the 60 wt.% WS_2 content measured by SEM-EDS and TEM-EDS. In attempting to

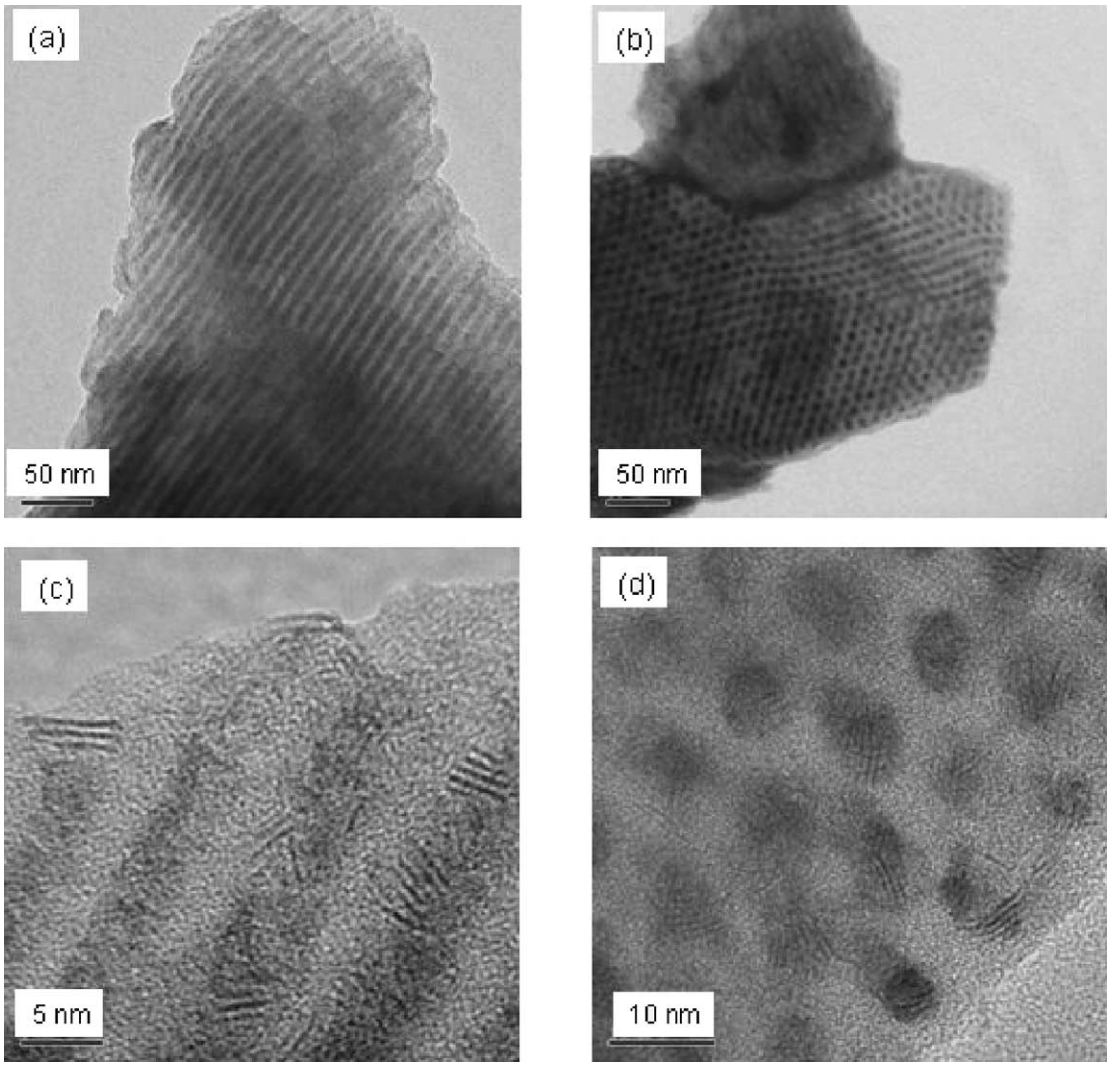

Fig. 4. TEM micrographs of the 60 wt.% WS_2/SBA-15 sample.

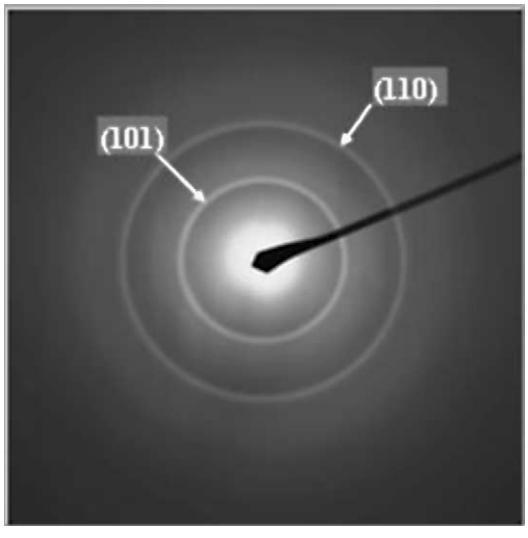

Fig. 5. Electron diffraction pattern from the 60 wt.% WS_2/SBA-15 sample.

explain this result, it is important to be aware of the fact that in electron microscopy the best contrast from the crystalline WS_2 nanoparticles is usually obtained when they are oriented in the (0001) plane parallel to the electron beam, which facilitates the observation of the 6.2-Å spacing. This means that for normal random space orientation of the slabs, only part of the slabs could be visible by TEM. This situation is shown schematically in Figs. 7b and 7c, in which it is assumed that the electron beam is perpendicular to the plane containing the nanotubes. Only three WS_2 particles are visible in a side view of the nanotubes actually containing four WS_2 particles (Fig. 7c). It is clear, however, that the "invisible" particle would be visible at a different orientation of the electron beam relative to the sample. Thus, different WS_2 slabs within a nanotube will become visible as the orientation of the specimen is changed. A series of HRTEM images recorded at different tilts (−10°, 0°, and +10°) for the same area of specimen are shown at Fig. 8. Comparison of the images of the same nanotubes (marked by the same numbers in Figs. 8a–8c) obtained at different orientations

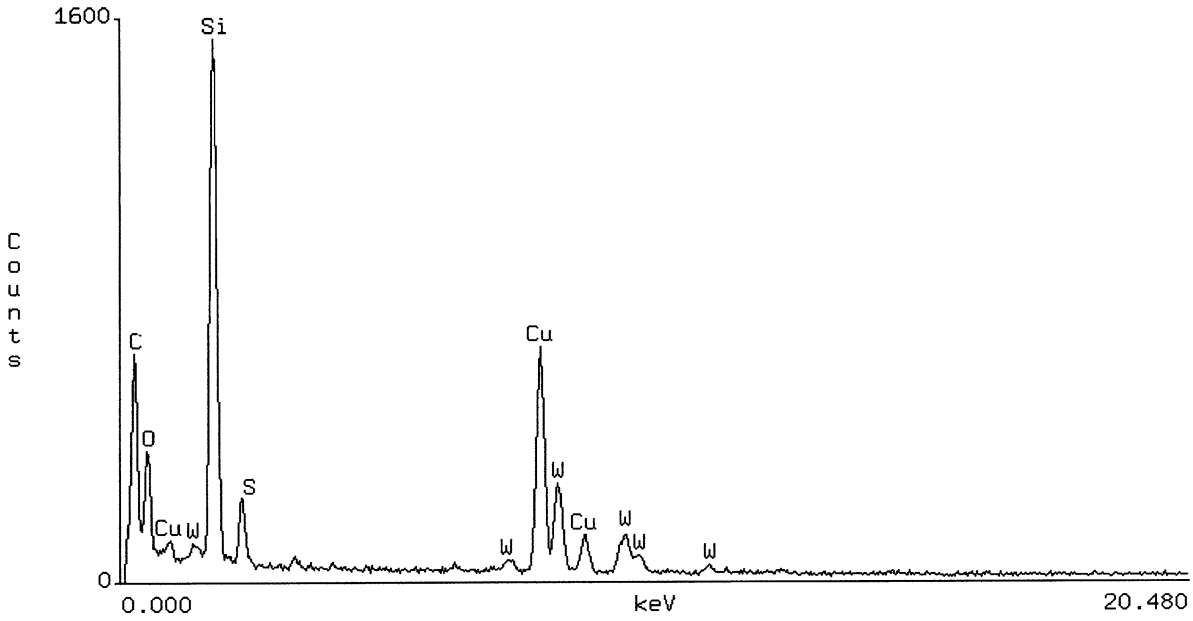

Fig. 6. Typical EDS spectrum taken from the 60 wt.% WS_2/SBA-15 sample.

clearly demonstrated that some WS_2 slabs will disappear and others will appear in certain places in a nanotube. This could explain the fact that the above-described calculations underestimated the WS_2 content. The same calculations based on Eqs. (1) and (3) that took into account all the visible WS_2 slabs at different orientations ($-10°$, $0°$ and $+10°$) yielded 30 wt.% WS_2 content rather than 60 wt.% of that measured by EDS. It is thus reasonable to assume that further tilting at higher angles, which was not possible because of the disappearance of the clear image of the nanotubes, would have increased the "visible" concentration up to that measured by EDS. These findings thus imply that the entire WS_2 phase exists in the form of well-crystallized nanoslabs, in agreement with the XRD results.

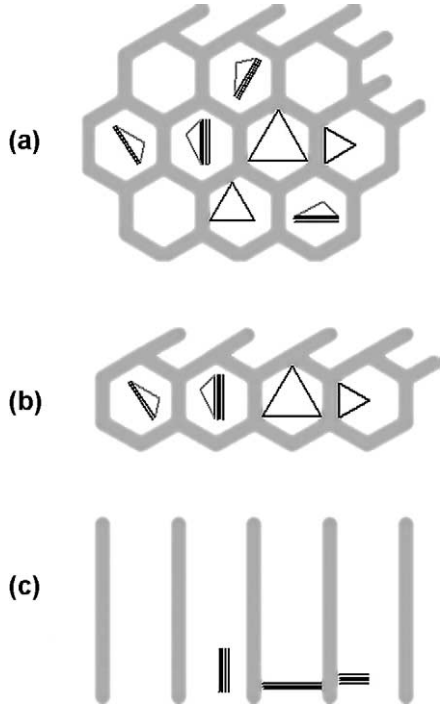

Fig. 7. Model of WS_2 nanoslabs inserted into the SBA-15 nanotubes (a), the thin place in the sample (b), side view of the thin place in the sample (c).

3.2. Mechanism of WS_2 insertion to the mesopores under ultrasonication

The effective insertion of WS_2 into mesoporous silica SBA-15 by means of ultrasonication can be related to the cavitation phenomena (i.e., formation, growth, and implosive collapse of the bubbles) as well as to the effects of propagation of acoustic waves in the liquids. In the first stage of the process, WS_2 nanoclusters are formed as a result of the high temperature processes inside the cavitating bubble. The resonance radius of the collapsing bubbles is estimated at about 100–150 μm at the ultrasonic frequency of 20 kHz. Thus, the bubbles cannot collapse inside the mesopores, which have a diameter of about 6.5 nm. However, bubble collapse in the liquid generates intensive shock waves, and the transient high pressure from the shock waves probably prevents plugging of the nanotubules of the mesoporous silica with the WS_2 precipitate. In addition, it is well known that ultrasound waves generate acoustic pressure P_{ac} in the liquid [39]. The value of P_{ac} is proportional to the intensity I, of the ultrasound; i.e., $P_{ac} = (2\rho c)^{1/2}(I)^{1/2}$, where ρ is the density of the liquid and c is the velocity of sound in this liquid. P_{ac} can reach several bars at the ultrasonic intensities of about 40–60 W/cm^2 used in the present work. P_{ac} causes an acoustic capillary effect; i.e., the rate of liquid streaming is considerably accelerated inside

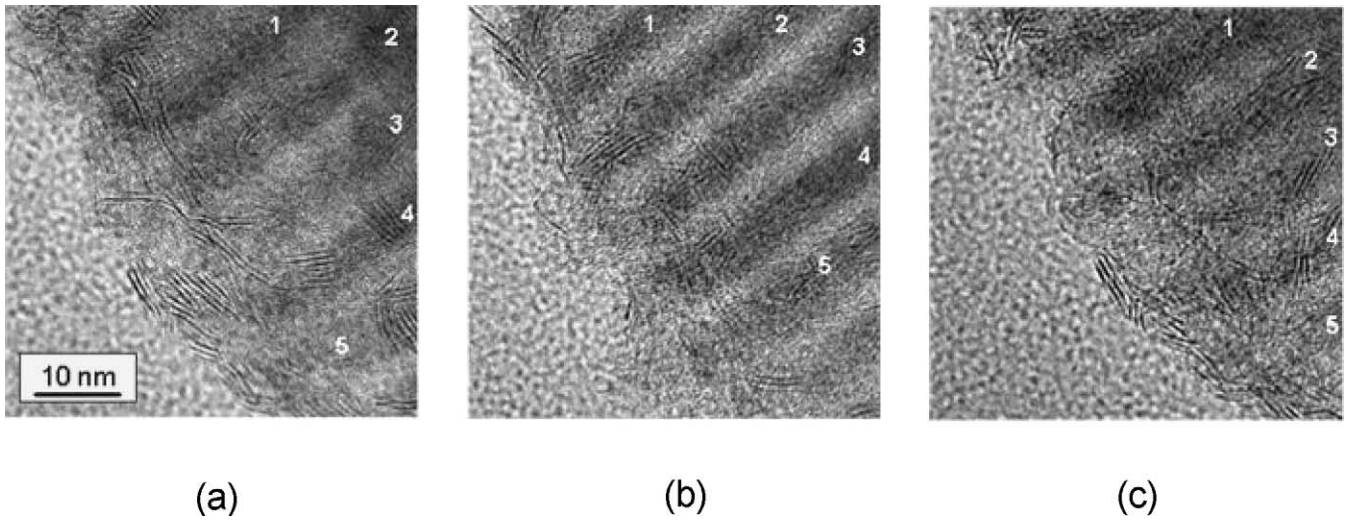

Fig. 8. HRTEM images recorded at different tilts for the same area of a specimen: (a) −10°; (b) 0°; (c) +10°.

the thin capillaries under the effect of ultrasound, even in the absence of cavitation.

The microjet phenomenon provided by the asymmetrical collapse near an extended solid–liquid interface most probably plays only a very minor role in the studied process, since the size of the SBA-15 particle (∼ 1.0 μm, based on TEM measurements in agreement with value reported in [29]) is much less than the resonance radius of the cavitating bubble. Microjets are not generated under such conditions.

The following mechanism may be proposed for WS_2 insertion into the nanotubular pores of SBA-15:

(i) WS_2 colloids are formed due to collapse of the bubbles. The particle size of the colloidal WS_2 precursor is assumed to be about 1–2 nm.
(ii) The colloidal WS_2 precursor is pushed inside the mesopores under the acoustic pressure created by the propagation of ultrasonic waves and the shock waves from the collapsing bubbles.
(iii) The inserted WS_2 nanoparticles are precipitated on the internal walls of the mesopores. Microstreaming and acoustic shock waves prevent blockage of the nanocapillaries.
(iv) Subsequent "sulfidation" treatment causes crystallization of nanoparticles into well-defined layered nanoslabs.

3.3. HYD/HDS performance of WS_2/SBA-15 and Ni–WS_2/SBA-15 catalysts

Assuming that the catalyst with the maximum W-loading would display the highest HDS and HYD activity, the WS_2/SBA-15 sample with a WS_2 content of 60 wt.% (W/Si = 0.36) was selected for testing the effect of the Ni/W ratio on the rates of HDS of DBT and HYD of toluene (Fig. 9). Increasing the Ni content in the catalyst increased both HDS and HYD catalyst activity up to an Ni/W ratio of about 0.4, followed by a slight decrease at Ni/W ratio of 0.8. The well-known promotion effect in the Co–Mo–S system has been observed in many sulfide systems at a Co/Mo ratio of about 0.5 [13,14]. Ni–W–S is expected to have a similar optimal Ni/W ratio. However, the optimal Ni/W ratio for supported Ni–W catalysts varied in a wide range from 0.6 to 2 [24,40–44], and was equal to 2 for a bulk Ni–W mixed sulfide system [45,46] obtained by sulfidation of oxide precursors. At high Ni/W ratios, a separated Ni_3S_2 phase is detected [24]. It thus seems that an excess of Ni in the mixed oxide system is needed to increase the degree of sulfidation of the tungsten phase. In the present work, the Ni promoter was introduced into the catalyst with the fully presulfided WS_2. As a result, the optimal Ni/W ratio was equal to that needed for formation of an active Ni–W–S phase without an excess of Ni_3S_2 in the mesopores of SBA-15 [32]. No separate Ni phase was detected by XRD up to a Ni/W atomic ratio of 0.8 (Fig. 3). In addition, the Ni component did not change the TEM-visible morphology of WS_2 slabs (neither the length nor the stacking number). TEM-EDS was employed to measure the chemical composition at several points of Ni–W–S/SBA-15 composite samples. All the EDS analyses collected from the different points gave an Ni/W ratio (average of 10 measurements) similar to the averaged composition measured by SEM-EDS. These measurements showed that the Ni component was distributed uniformly in the sample, probably decorating the edge planes of the WS_2 slabs.

Table 2 compares the HDS and HYD performances of the Ni–W–S/SBA-15 catalyst with those of a commercial Co–Mo/Al_2O_3 catalyst and of Ni–W catalysts deposited on conventional γ-Al_2O_3 and SiO_2 supports by impregnation, as was reported previously [24]. The W content in Ni–W catalysts on conventional supports and Ni/W ratio was shown to be optimal for these systems [24].

For proper comparison of the catalytic performance of active phases deposited at different supports, possible diffu-

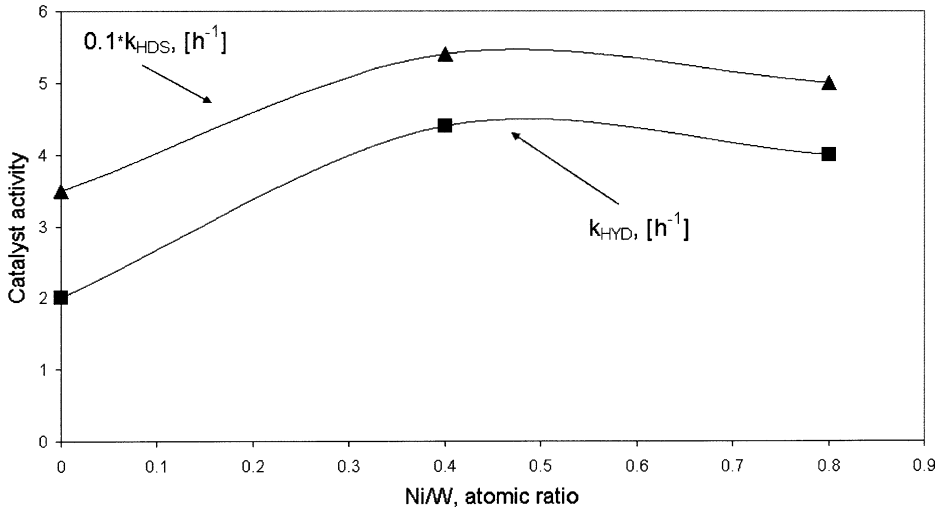

Fig. 9. Performance of Ni–W–S/SBA-15 catalysts in DBT HDS and toluene HYD (W/Si = 0.36 and different Ni contents).

sion limitation should be considered. This is especially important for the Ni–W–S/SBA-15 catalyst in which the slabs located in the mesopores could decrease the pore diameter. However, as was shown earlier, the volume of the WS_2 phase in 60 wt.% WS_2/SBA-15 sample was only about 20% (0.08/0.4) of the pore volume of the SBA-15 support. This is confirmed by the fact that the pore diameter of the 60 wt.% WS_2/SBA-15 sample was decreased only to a minor extent in comparison with the parent SBA-15 (Fig. 2b), since the starting N_2-sorption, before the phase transition to liquid nitrogen, occurred mainly at the walls of SBA-15 in the 60 wt.% WS_2/SBA-15 sample and not on the WS_2 phase. The slabs located within the mesopores could constitute sudden reductions of the pore size, thus increasing the diffusion resistance. The preliminary calculation of the Thiele modulus was performed using the molecular diffusion coefficient of DBT in a decane–octadecane reaction mixture, as calculated by the Wilke–Chang correlation [47]. Under the reaction temperature (593 K), the diffusion coefficient was equal to 2×10^{-4} cm^2/s. The effective diffusion coefficient inside the pore is normally lower by an order of magnitude than the molecular diffusion coefficient due to the porosity and pore tortuosity of the catalyst pellet [48]. Taking an effective diffusion coefficient of 2×10^{-5} cm^2/s, a catalyst pellet diameter of 1.3 mm, and a zero-order HDS rate constant normalized with the initial DBT concentration $k_{HDS} = k/C_0$ (C_0 is the inlet DBT concentration; k is the pseudo-zero-order HDS rate constant) of 54 h^{-1} (Table 2), a Thiele modulus of 0.4 was calculated. This means that diffusion effects for the zero-order DBT HDS reaction can be neglected. For the gas-phase toluene HYD reaction, the bulk diffusion coefficient was estimated by the Fuller correlation [47] to be 0.02 cm^2/s. The Knudsen diffusion coefficient inside the catalyst pores was estimated according to simple kinetic theory [48] to be 0.008 cm^2/s. Combining the bulk and Knudsen diffusion coefficients, we obtained the resulting diffusion coefficient inside the pores as equal to 0.006 cm^2/s. Taking the effective diffusion coefficient to be an order of magnitude lower, i.e., 6×10^{-4} cm^2/s, a catalyst pellet diameter of 1.3 mm, and a first-order HYD rate constant of 4.4 h^{-1} (Table 2), we obtained a Thiele modulus of 0.03. Thus, no diffusion limitations were present. Experimental work is currently under way to measure the effective diffusion coefficients.

The HDS activity of the SBA-15 supported Ni–W–S catalyst was higher than that of commercial Co–Mo catalyst (Table 2). Such finding is reported for the first time because it is commonly accepted that W-based catalysts are less efficient in HDS reactions but more efficient in aromatic HYD than Mo-based catalysts [13,34,49]. Indeed the TON (HDS) value of the Ni–W–S/SBA-15 catalyst is lower than that of the commercial Co–Mo catalyst, in agreement with the higher specific HDS efficiency of Mo than of W. However, the very high percentage of WS_2 in the Ni–W–S/SBA-15

Table 2
Comparison of catalysts' performance in dibenzothiophene HDS and toluene HYD

Catalyst	W(Mo) (wt%)	Ni(Co) (wt%)	Particle length[a] (nm)	Stacking number[a]	k_{HYD} (h^{-1})	k_{HDS} (h^{-1})	TON_{HDS} (h^{-1})
Co–Mo/Al_2O_3 commercial catalyst	17.6	4.5	–	–	0.6	38	1.26
Ni–W–S/SBA-15	44.5	5.7	3.6	3.2	4.4	54	0.90
Ni–W/SiO_2	26.9	16.6	7.7	5.1	5.8	28	0.74
Ni–W/Al_2O_3	26.4	16.4	7.3	2.4	0.9	28	0.78

[a] Average value obtained from HR-TEM statistics.

catalyst makes it more efficient in HDS than the commercial Co–Mo catalyst, yielding higher DBT conversions for the same volume of catalyst loaded into the reactor.

As a result of high percentages of WS_2 in the Ni–W–S/SBA-15 catalyst, it was much more efficient in HDS than silica- or alumina-supported Ni–W catalysts. Furthermore, the TON (HDS) value of the Ni–W–S/SBA-15 catalyst is higher than that of silica- or alumina-supported Ni–W catalysts. The higher specific activity of WS_2 supported on SBA-15 is probably a consequence of the fact that WS_2 slabs are much shorter on SBA-15 than on conventional supports (Table 2). Shorter slabs provide higher amounts of edge planes, thus increasing the WS_2 specific activity.

Ni–W–S/SBA-15 catalyst, as expected, displayed HYD activity 7.3 times higher then the commercial Co–Mo/Al_2O_3 (Table 2). The HYD activity of the Ni–W–S/SBA-15 catalyst is lower than that of silica-supported Ni–W and higher than that of alumina-supported catalyst (Table 2). As we recently reported [24], the higher HYD activity of silica-supported Ni–W is a result of the higher stacking number of WS_2 slabs compared with the alumina-supported catalyst. This could be explained in terms of WS_2 loading and the dimensions of the WS_2 slabs, namely, slab length and stacking number. WS_2 slabs in SBA-15 are both shorter and thicker than WS_2 slabs on alumina. These structural features together with higher loading result in a higher HYD activity of Ni–W–S/SBA-15 catalyst than of Ni–W/Al_2O_3. In contrast, the stacking number of WS_2 slabs on silicagel is higher than that on SBA-15. This seems to be the most important structural feature determining the HYD activity of the catalyst, since even with longer slabs and lower WS_2 loading, the silica-supported catalyst is more active in HYD than the Ni–W–S/SBA-15 catalyst. However, being very efficient in HDS and having quite high HYD activity, the high-loading Ni–W–S/SBA-15 catalyst has excellent potential for application in deep HDS of petroleum feedstocks [49].

4. Summary

In the present study, layered nanoslabs of a WS_2 phase with a well-defined hexagonal crystalline structure were inserted into the nanotubular channels of an ordered pure-silica SBA-15 at loadings up to 60 wt.%. Sonication of a slurry containing SBA-15 material in a $W(CO)_6$–sulfur–diphenylmethane solution yielded an amorphous WS_2 phase inside the mesopores. The proposed mechanism of WS_2 insertion to the mesopores under ultrasonication combines two phenomena—cavitation and propagation of acoustic waves in a liquid, i.e., WS_2 nanoparticles, which are formed due to collapse of the bubbles, are pushed inside the mesopores under the acoustic pressure created by the propagation of ultrasonic waves and the shock waves from the collapsing bubbles. The resulting amorphous WS_2 phase is transformed into hexagonal crystalline WS_2 nanoslabs by treatment with a 1.5% DMDS–toluene mixture at 593 K and 5.4 MPa under a hydrogen flow (XRD, HRTEM, SAED).

The WS_2 nanoslabs were uniformly distributed exclusively inside the mesopores (HRTEM, EDS) and oriented with their edge planes toward the support surface. At 60 wt.% loading, the volume of the WS_2 phase was only about 20% of the pore volume of the SBA-15 support, and the blocking extent of the mesopores was minimal (N_2-sorption). The clear HRTEM images of the well-defined crystalline catalytic WS_2 phase inside the SBA-15 nanotubes are the first of their kind ever to be reported in the literature. Furthermore, a combination of the three requirements for efficient catalytic phase dispersion mentioned in the Introduction, i.e., high loading of a well-defined crystalline catalytic phase exclusively in the nanotubular channels of mesoporous silica without blocking of the channels, was achieved for the first time in the present study.

The Ni component was introduced into the WS_2/SBA-15 composite by impregnation with an aqueous solution of nickel acetate, drying under vacuum at room temperature and sulfidation. Increasing the Ni content in the catalyst increased both HYD and HDS activity up to Ni/W ratio of about 0.4 followed by a slight decrease at Ni/W ratio of 0.8. The Ni component was uniformly dispersed (HRTEM, XRD). The optimized Ni–W–S/SBA-15 catalysts displayed 1.4 times higher HDS activity (DBT) and 7.3 times higher activity in toluene HYD compared with sulfided commercial Co–Mo/Al_2O_3. This points to the excellent potential of the high-loading Ni–W–S/SBA-15 catalyst for deep hydrotreating of petroleum feedstocks.

Acknowledgments

This research was supported by the Israel Academy of Sciences and Humanities. The authors thank Dr. A.I. Erenburg and Dr. S. Pevzner for assistance in XRD and SAXS characterizations, respectively.

References

[1] U. Ciesla, F. Schüth, Micropor. Mesopor. Mater. 27 (1999) 131.
[2] G. Øye, J. Sjöblom, M. Stöcker, Adv. Colloid. Interface Sci. 89–90 (2001) 439.
[3] J.C. Jansen, Z. Shan, L. Marchese, W. Zhou, N.V.D. Puil, Th. Maschmeyer, Chem. Commun. (2001) 713.
[4] K. Moller, T. Bein, Chem. Mater. 10 (1998) 2950.
[5] D. Brunel, Micropor. Mesopor. Mater. 27 (1999) 329.
[6] A. Corma, Top. Catal. 4 (1997) 249.
[7] F. Schuth, A. Wingen, J. Sauer, Micropor. Mesopor. Mater. 44–45 (2001) 465.
[8] B.M. Reddy, I. Ganesh, B. Chowdhury, Catal. Today 49 (1999) 115.
[9] M. Gasior, J. Haber, T. Machej, Appl. Catal. A 33 (1987) 1.
[10] F.R. Chen, G. Coudurier, J.F. Joly, J.C. Verdine, J. Catal. 143 (1993) 616.
[11] R.A. Comelli, C.R. Vera, J.M. Parera, J. Catal. 151 (1995) 96.
[12] D. Farcasiu, J.Q. Li, S. Cameron, Appl. Catal. A 154 (1997) 173.
[13] H. Topsøe, B.S. Clausen, F.E. Massoth, in: J.R. Anderson, M. Boudart (Eds.), Hydrotreating Catalysis, Springer, Berlin, 1996.
[14] D.D. Whitehurst, T. Isoda, I. Mochida, Adv. Catal. 42 (1998) 345.
[15] J.V. Lauritsen, S. Helveg, E. Laegsgaard, I. Stensgaard, B.S. Clausen, H. Topsøe, F. Besenbacher, J. Catal. 197 (2001) 1.

[16] J.B. Nagy, P. Bodart, I. Hannus, I. Kiricsi, Synthesis, Characterization and Use of Zeolitic Microporous Materials, DecaGen Ltd., Szeged-Szöred, 1998.
[17] N. Mizuno, M. Misono, Chem. Rev. 98 (1998) 199.
[18] J. Sauer, F. Marlow, B. Spliethoff, F. Schüth, Chem. Mater. 14 (2002) 217.
[19] M. Froba, R. Köhn, G. Bouffaud, Chem. Mater. 11 (1999) 2858.
[20] A. Ghanbari-Siahkali, A. Philippou, J. Dwyer, M.W. Anderson, Appl. Catal. A 192 (2000) 57.
[21] M.V. Landau, E. Dafa, M.L. Kaliya, T. Sen, M. Herskowitz, Micropor. Mesopor. Mater. 49 (2001) 65.
[22] A. Goldbourt, M.V. Landau, S. Vega, submitted for publication.
[23] M.V. Landau, L. Vradman, M. Herskowitz, Y. Koltypin, A. Gedanken, J. Catal. 201 (2001) 22.
[24] L. Vradman, M.V. Landau, Catal. Lett. 77 (2001) 47.
[25] E.J.M. Hensen, P.J. Kooyman, Y. van der Meer, A.M. van der Kraan, V.H.J. de Beer, J.A.R. van Veen, R.A. van Santen, J. Catal. 199 (2001) 224.
[26] Y. Skashita, Y. Araki, K. Honna, H. Shimada, Appl. Catal. 197 (2000) 247.
[27] A. Gedanken, X. Tang, Y. Wang, N. Perkas, Yu. Koltypin, M.V. Landau, L. Vradman, M. Herskowitz, Eur. J. Chem. 7 (2001) 4546.
[28] S. Nikitenko, Y. Koltypin, Y. Mastai, M. Koltypin, A. Gedanken, J. Mater. Chem. 12 (2002) 1450.
[29] D. Zhao, J. Feng, Q. Huo, N. Melosh, G.H. Fredrickson, B.F. Chmelka, G.D. Stucky, Science 279 (1998) 548.
[30] D. Zhao, J. Sun, Q. Li, G.D. Stucky, Chem. Mater. 12 (2000) 275.
[31] M. Imperor-Clerc, P. Davidson, A. Davidson, J. Am. Chem. Soc. 122 (2000) 11925.
[32] M.V. Landau, L.I. Nikulina, B.K. Nefedov, A.A. Slinkin, React. Kinet. Catal. Lett. 25 (1–2) (1984) 115.
[33] M.V. Landau, M. Herskowitz, D. Givoni, S. Laichter, D. Yitzhaki, Fuel 77 (1998) 3.
[34] L. Vradman, M.V. Landau, M. Herskowitz, Catal. Today 48 (1999) 41.
[35] R.C. Weast, M.J. Astle, CRC Handbook of Chemistry and Physics, 62nd ed., CRC, New York, 1982.
[36] Powder Diffraction Files, JCPDS, International Center for Diffraction Data, 1984.
[37] J. Sauer, F. Marlow, F. Schuth, Phys. Chem. Chem. Phys. 3 (2001) 5579.
[38] A.N. Startsev, Catal. Rev. Sci. Eng. 37 (1995) 353.
[39] D.E. Gray, American Institute of Physics Handbook, 3rd ed., McGraw–Hill, New York, 1972.
[40] M. Breysse, J. Bachelier, J.P. Bonnelle, M. Cattenot, D. Cornet, T. Decamp, J.C. Duchet, R. Durand, P. Engelhard, R. Frety, C. Gachet, P. Geneste, J. Grimblot, C. Gueguen, S. Kasztelan, M. Lacroix, J.C. Lavalley, C. Leclercq, C. Moreau, L. de Mourgues, J.L. Olivé, E. Payen, J.L. Portefaix, H. Toulhoat, M. Vrinat, Bull. Soc. Chim. Belg. 96 (1987) 829.
[41] M.J. Vissenberg, Y. van der Meer, E.J.M. Hensen, V.H.J. de Beer, A.M. van der Kraan, R.A. van Santen, J.A.R. van Veen, J. Catal. 198 (2001) 151.
[42] C.H. Kim, W.L. Yoon, I.C. Lee, S.I. Woo, Appl. Catal. 144 (1996) 159.
[43] T. Kabe, W. Qian, A. Funato, Y. Okoshi, A. Ishihara, Phys. Chem. Chem. Phys. 1 (1999) 921.
[44] R.E. Tischer, N.K. Narain, G.J. Stiegel, D.L. Cillo, Prepr. Am. Chem. Soc. Div. Pet. Chem. 30 (1985) 459.
[45] O. Weisser, S. Landa, Sulfide Catalysts, Their Properties and Applications, Pergamon, London/Oxford, 1973.
[46] L.N. Alexeenko, M.V. Landau, V.Ya. Kruglikov, B.K. Nefedov, Kinet. Katal. 25 (1984) 630.
[47] R.C. Reid, J.H. Prauznitz, T.K. Shervood, The Properties of Gases and Liquids, 4th ed., McGraw–Hill, New York, 1987.
[48] J.M. Smith, Chemical Engineering Kinetics, 3th ed., McGraw–Hill, Tokyo, 1981.
[49] M.V. Landau, Catal. Today 36 (1997) 393.